

Theoretical Investigation of Temperature and Grain Size Dependence of Thermal Properties of alpha-Silicon Crystal

Nenuwe O.N.

Department of Physics, Federal University of Petroleum Resources,
P. M. B. 1221, Effurun, Delta State, Nigeria
nenuwe.nelson@fupre.edu.ng

Abstract: Using reverse non-equilibrium molecular dynamics method, we study the thermal properties of grain boundary between two alpha-silicon crystal grains with (200) and (220) crystallographic orientations. The interfacial thermal conductance of the grain boundary and thermal conductivity are temperature dependent, leading to increasing/decreasing thermal transport as the temperature is increased. Also, thermal conductivity increased with increasing grain size. The observed decrease in thermal resistance indicates the suitability of silicon as interface materials for high-thermal conductivity material applications and thermal management in micro and nanoelectronic devices.

Introduction

The desire for faster and cheaper electronic devices, continuous device miniaturization and increasing density of components on an integrated circuit has increased the complexity of micro- and nanoelectronics [1– 6]. It is well known that downsizing of electronic devices has enhanced computing capabilities at the expense of increasing heat dissipation across the material [7–9]. This has posed great

thermal management challenge within the electronic device industry. Over the past fifty years [10], it has motivated material scientists and engineers into rigorous research and continuous development of new materials, by making thermal designs an integral part of the fabrication of electronic devices to increase computing performance. For example, in some processor modules, the power required for high-performance

computing (HPC) may reach 300 – 400W resulting to heat loads up to 4kW for processors in a ten-socket computing system [11]. High management of power dissipation has great implications on such systems, and therefore, requires good thermal management solutions that will quickly transfer the heat from hot spots to regions of low temperature to maintain high reliability of such electronic device. According to Panasonic [12], energy consumption rate keeps increasing even as the size of electronic devices is continuously decreasing, and the usual techniques for thermal transfer have failed to meet the present day electronic designs. Hence, they developed the Pyrolytic graphite sheet (PGS) for thermal management solutions. The PGS was designed to diffuse heat generated by heat sources like power amplifier, computer processors, and batteries. Also, Tang et al. [13] reiterated that thermal interface materials which are usually introduced to bridge the gap between difficulties to minimize the thermal contact resistance can capably improve heat dissipation of electronic devices [14]. It is important to note that thermal conductivity is difficult to predict when the electronic device is fabricated from different materials. Therefore, material scientists and engineers are always designing interfaces between materials to minimize or maximize thermal conductivity [15].

Thus, in this review article, we use the reverse non-equilibrium molecular dynamics (RNEMD) [16] with a classical potential to simulate the heat

flow through alpha-silicon (200) and (220) interface and calculate the interfacial Kapitza conductance and resistance of the grain boundary at different temperatures. The thermal conductivity is calculated at all temperatures, and the grain-size dependence of thermal conductivity is also investigated to have more insight into the behavior of thermal conductivity as the grain size is varied.

This article is arranged as follows: Section 2 briefly reviews the theory of RNEMD and discusses the computational details. The results obtained are analyzed in Section 3, and Section 4 discusses the conclusion of the study.

Theory and Computational methods

The interfacial thermal conductance is calculated with the reverse non-equilibrium molecular dynamics method. In this method heat flux dQ/dt is imposed through two alpha-silicon crystal grains with (200) and (220) crystallographic orientations, which results in temperature jump (ΔT) across the grain boundary since the interface creates additional thermal resistance, R to the heat flow, and a temperature gradient is generated over the hot and cold grains as illustrated in Figure 1. The thermal conductance (G) across an interface, also called Kapitza conductance [17] is directly proportional to the heat flux and inversely proportional to the temperature jump developing across the grain boundary as given by Eq. (2.1)

$$G = \frac{dQ/dt}{\Delta T} = \frac{1}{R} \quad (2.1)$$

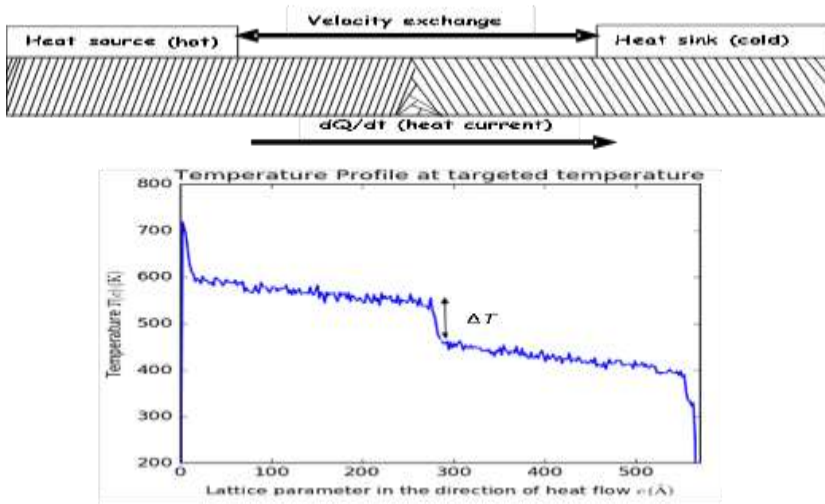


Figure 1. A diagram of simulation system for determining thermal conductivity across the interface of two silicon crystals in (200) and (220) crystallographic orientations in the regime of RNEMD technique.

In Figure 1, the heat flux is imposed by periodically exchanging the positions and velocities of the hottest atoms in the heat sink (cold grain) and coldest atoms in the heat source (hot grain). After the exchange, the velocities of the atoms in the cold and hot grains are given as [18]

$$v'_c = -v_c + 2 \left(\frac{m_c v_c + m_h v_h}{m_c + m_h} \right) \quad (2.2)$$

$$v'_h = -v_h + 2 \left(\frac{m_c v_c + m_h v_h}{m_c + m_h} \right) \quad (2.3)$$

Where v_c and v_h are velocities of atoms before the exchange, v'_c and v'_h are velocities after the exchange in the cold and hot grains, m_c and m_h are the respective masses for the cold and hot atoms. This results in heat flow from the heat source to the heat sink. Because of energy conservation and the buildup of a temperature gradient, energy transport is generated in the opposite direction. When adequate exchange has occurred, a steady-state heat flux, dQ/dt is reached in the

system, and it is directly proportional to the magnitude (but opposite in direction) of the temperature gradient, dT/dz as given by Eq. (2.4). Where κ , is the thermal conductivity of the material, and A , is the area perpendicular to heat flux.

$$\frac{dQ}{dt} = -\kappa A \frac{dT}{dz} \quad (2.4)$$

In this study, the virtual nanolab 2017.1 [19] is used to prepare grain boundary between two α -silicon (Si) crystal grains with (200) and (220) crystallographic orientations. The thermal current is directed to run along the z-direction. The (200) and (220) crystal grain interface are studied for $(A_x X B_y X C_z =)$ 11.52X11.52X570, 11.52X11.52X680, 15.3601X15.3601X270 and 15.3601X15.3601X550 supercells. The C_z -vector was chosen to be larger than A_x and B_y because in the non-equilibrium thermal current simulations, it is customary to choose a large cell length in the direction of heat flow. The supercell created is

non-periodic in the C_z -direction so as to terminate the system by vacuum at either end. Then, the slab is centered in the middle of the supercell.

The atomistix toolkit (ATK) force field calculator [19-21] and Stillinger-Weber potential [22] are used for the equilibration of the system. The system is first optimized using LBFGS method [23] with a tolerance of 0.1eV/Å and 0.1GPa in stress error, to remove initial large destabilizing forces that might have occurred during the interface generation. Then, the lateral cell vectors are relaxed and equilibrated to the target temperature using the molecular dynamics (MD) method. First, the thermal transport simulation is performed at an average temperature of 500K. The molecular dynamics type is taken as NPT Martyna-Tobias-Kelein [24]. The simulation is carried out for 7×10^4 steps at log interval of 1.5×10^3 . External stress is switched off and reservoir temperature is set to 500K. In order to remove the center of mass momentum, the initial velocity is set to Maxwell Boltzmann distribution at 500K. These settings are used to carry out the simulation at constant temperature and pressure. When the simulation is done, the grains of the resulting structure is now relaxed and equilibrated at 500K. For the equilibrated structure, regions of the

heat source and heat sink are defined within the (200) and (220) oriented grains. The NVT Nose Hoover Chain [25] type MD is then used to equilibrate the system at constant volume. To achieve this, the simulation is carried out for 1×10^5 steps at log intervals of 1×10^4 to allow the system to reach steady-state regime. Reservoir and final temperatures are set to 500K, and thermo-state time scale is taken to be 100fs.

Finally, another MD block is used to carry out the non-equilibrium simulations. Here, we set MD type to non-equilibrium momentum exchange, the number of simulation steps and log interval are taken as 8×10^5 and 2000, respectively. The configuration velocities are used. The time step is set to 1fs. The exchange interval is taken as 200. This is to allow the exchange to stimulate every 200 steps and to increase the transferred kinetic energy per simulation time, which yields larger temperature gradient and a more definite temperature profile. When the simulation is done, the system is carefully checked for convergence with respect to the system size and simulation time. Subsequently, the entire simulation is repeated at other temperatures 600K, 800K and 1000K, respectively

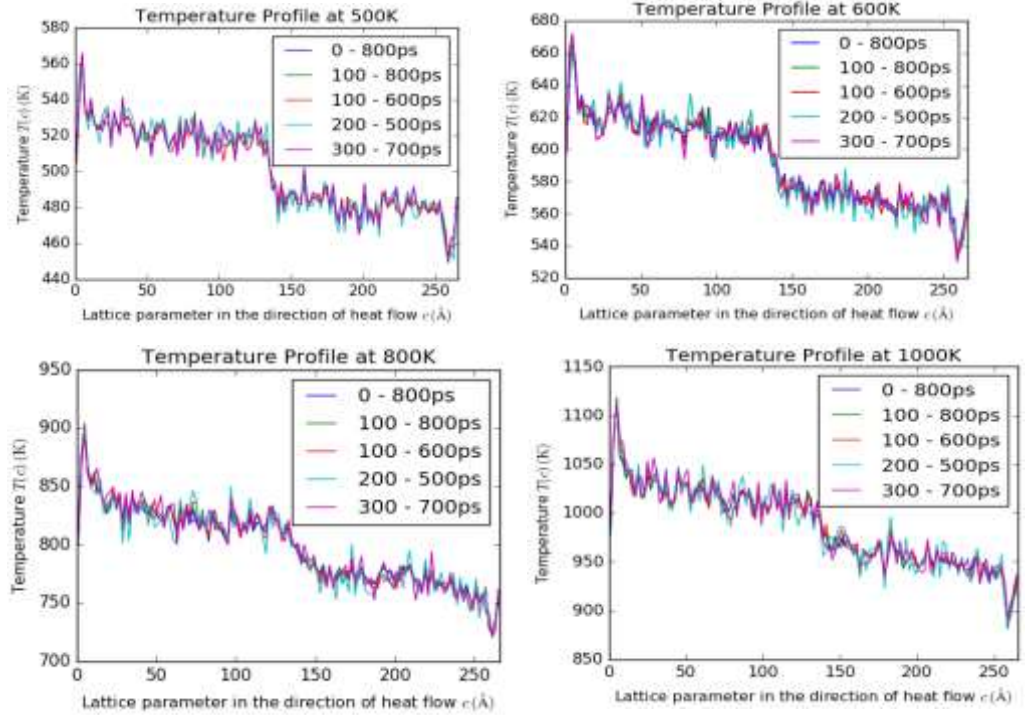


Figure 2. Comparison of temperature profile between 0 - 800ps, 100 - 800ps, 100 - 600ps, 200 - 500ps and 300 - 700ps at different temperatures: 500K, 600K, 800K and 1000K.

Result Analysis

First, we check the convergence of the temperature profile with respect to the simulation time. This is done by comparing different time intervals with one another. The temperature profile is shown in Figure 2. The blue, green, red, sky-blue and purple curves correspond to the intervals, 0 – 800 picosecond (ps), 100 - 800ps, 100 - 600ps, 200 - 500ps and 300 – 700ps, respectively. In Figure 2, it can be seen that the curves in the temperature profile are in a steady state. That is, the temperature profile looks the same as time passes. This implies that the temperature profile for 500K, 600K, 800K and 1000K converged with respect to the simulation time. The temperature profile shows positive and negative peaks on the left and right-hand sides of the profile. These areas

respectively, signify the heat source and heat sink. This non-linear section comes from the artificial transfer of kinetic energy due to the momentum exchange between the hot and cold grains.

For the system with lattice parameters 11.52X11.52X570, around $C_z = 274\text{Å}$, there is a temperature jump $\Delta T = 106\text{K}$. This is the interface region that provides additional thermal resistance. From our simulation, the average heat flux at 500K is 0.00082eV/fs. Therefore, the Kapitza conductance is obtained from Eq. (2.1) as

$$G = \frac{dQ/dt}{\Delta T} = \frac{0.00082 \times (1.6 \times 10^{-19} \text{J})}{(106\text{K})(10^{-15} \text{s})} = 1.2377 \times 10^{-9} \text{ J/sK or (WK}^{-1}\text{)} \quad (3.1)$$

This implies that the interface between the temperature source and sink causes a discontinuity in the temperature

profile since the interface provides thermal resistance of $R = 1/G = 8.0795 \times 10^8 \text{ KW}^{-1}$, to the heat current. At 600K, $C_z = 276 \text{ \AA}$ and the temperature jump is $\Delta T = 116 \text{ K}$. The average heat flux is obtained as 0.00099 eV/fs . Therefore, the thermal or Kapitza conductance is obtained as $1.3655 \times 10^9 \text{ WK}^{-1}$, and the interfacial thermal

resistance is $7.3232 \times 10^8 \text{ KW}^{-1}$. Tables 1 – 4 show the average heat flux, temperature jump, Kapitza conductance and interface thermal resistance at different temperatures for the various systems considered. As we can observe, the Kapitza conductance and interface thermal resistance are sensitive to temperature.

Table 1 The Kapitza conductance (G), interface thermal resistance (R), temperature jump (ΔT) and average heat flux (dQ/dt) at different temperatures for (200) oriented grains in the system with lattice parameter $11.52 \times 11.52 \times 570$.

Temperature (K)	$C_z(\text{\AA})$	$\Delta T(\text{K})$	$dQ/dt \text{ (eV/fs)}$	$G(\text{WK}^{-1}) \times 10^{-9}$	$R(\text{KW}^{-1}) \times 10^8$
500	274	106	0.00082	1.2377	8.0795
600	276	116	0.00099	1.3655	7.3232
800	276	113	0.001272	1.8011	5.5522
1000	275	141	0.001488	1.6885	5.9224

Table 2 The Kapitza conductance (G), interface thermal resistance (R), temperature jump (ΔT) and average heat flux (dQ/dt) at different temperatures for (200) oriented grains in the system with lattice parameter $11.52 \times 11.52 \times 680$.

Temperature (K)	$C_z(\text{\AA})$	$\Delta T(\text{K})$	$dQ/dt \text{ (eV/fs)}$	$G(\text{WK}^{-1}) \times 10^{-9}$	$R(\text{KW}^{-1}) \times 10^8$
500	322	122	0.001321	1.7325	5.7720
600	324	168	0.001557	1.4828	6.7439
800	323	186	0.001958	1.6843	5.9372
1000	326	184	0.002478	2.1548	4.6408

Table 3 The Kapitza conductance (G), interface thermal resistance (R), temperature jump (ΔT) and average heat flux (dQ/dt) at different temperatures for (200) oriented grains in the system with lattice parameter $15.3601 \times 15.3601 \times 270$.

Temperature (K)	$C_z(\text{\AA})$	$\Delta T(\text{K})$	$dQ/dt \text{ (eV/fs)}$	$G(\text{WK}^{-1}) \times 10^{-9}$	$R(\text{KW}^{-1}) \times 10^8$
500	131	79	0.001068	2.1659	4.617
600	132	88	0.001275	2.3213	4.307
800	133	102	0.001688	2.6514	3.771
1000	136	136	0.002167	2.0303	4.925

Table 4 The Kapitza conductance (G), interface thermal resistance (R), temperature jump (ΔT) and average heat flux (dQ/dt) at different temperatures for (200) oriented grains in the system with lattice parameter $15.3601 \times 15.3601 \times 550$

Temperature (K)	$C_z(\text{\AA})$	$\Delta T(\text{K})$	$dQ/dt \text{ (eV/fs)}$	$G(\text{WK}^{-1}) \times 10^{-9}$	$R(\text{KW}^{-1}) \times 10^8$
500	276	64	0.001036	2.5900	3.8610
600	283	79	0.001237	2.5053	3.9915
800	279	77	0.001635	3.3974	2.9434
1000	279	161	0.002074	2.0611	4.8518

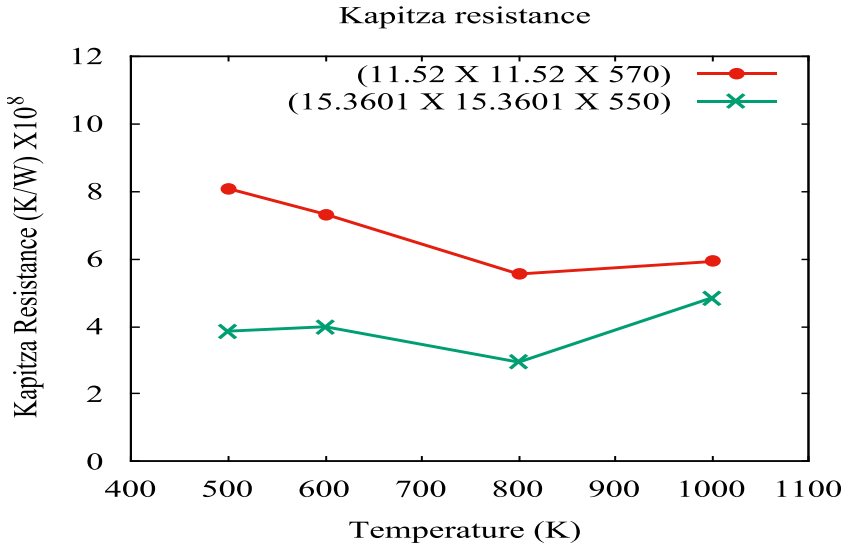


Figure 3. Interface Kapitza resistance as a function of temperature.

Usually, thermal resistance creates a barrier to heat flow leading to temperature jump across the interface [26,27]. Figure 3 displays the interface Kapitza resistance for the supercell crystal $11.52 \times 11.52 \times 570$, and $15.3601 \times 15.3601 \times 550$, as a function of temperature. As the temperature is increased from 500K to 1000K, the thermal resistance is observed to decrease linearly and then increased for $11.52 \times 11.52 \times 570$. While the interface resistance is observed to first increased as the temperature is increased from 500K to 600k, then decreased at 800K and finally, increased as the temperature is increased to 1000K for the $15.3601 \times 15.3601 \times 550$ supercell. This nonlinear behavior is as a result of the difference in discontinuity in the temperature profile at different temperatures. This trend has been obtained earlier by Song and Min [28], who pointed out that interface thermal resistance decreases with temperature

in the form $R = \frac{1}{\alpha}$, where α is higher for interface with weaker interactions. This significant property of silicon makes it suitable for use as interface material with other semiconductors in integrated circuit applications, with the aim to reduce or increase the thermal resistance across the boundary to allow the desired thermal transport and maintain an appropriate temperature within the electronic device.

Grain Size Dependence of Thermal Conductivity

Also, we calculated the grain size and temperature dependence of the thermal conductivity for the (200) and (220) crystallographic oriented grains. For the various supercells studied, the grain size dependence of the thermal conductivity is tabulated in Tables 5 – 8. Usually, the grain size dependence of thermal conductivity is modeled by the distance between the heat source or sink to the interface boundary. The thermal conductivity κ (W/mK) calculated for different temperatures at

different grain sizes displayed in Figure 4. It is obvious that thermal conductivity is sensitive to both temperature and grain size. For the (200) oriented grains, at each temperature in the four different supercells studied, it is seen that the thermal conductivity increased linearly between grain sizes 116 – 259 Å. Thereafter, there is a jump in thermal conductivity between grain sizes 257 – 270 Å, and then increased linearly again around 317 – 322 Å. A similar trend is also observed for the (220) oriented grains. This might be as a result of boundary effects in the system that is smaller than the mean free path of phonons [29].

Around the (200) oriented grains, at 500K in Tables 5 – 8, for the grain sizes 116, 250, 257 and 317 Å, we obtained the grain thermal conductivity as 29.209, 43.082, 51.18874 and 54.5233 W/mK, respectively. At 600K, for grain sizes 119, 257, 262 and 319 Å, the calculated grain thermal conductivity is respectively, 26.8058, 35.8068, 42.4583 and 47.6362 W/mK. At 800K, the simulated grain thermal conductivity for grain sizes 120, 258, 266 and 320 Å are 22.3884, 28.4109, 30.2294 and 33.1348 W/mK. Finally, at 1000K, for grain sizes 123, 259, 270 and 322 Å, the corresponding grain thermal conductivity is respectively, 15.1379, 18.9584, 22.0628 and 22.0947 W/mK.

Table 5. The grain size, temperature gradient dT/dz , and thermal conductivity κ , at different temperatures for (200) and (220) oriented grains in the system with supercell 15.3601 X 15.3601 X 270.

(200) oriented grains				(220) oriented grains		
Temperature (K)	Grain size (Å)	$dT/dz(K/\text{Å})$	$\kappa(WK^{-1}m^{-1})$	Grain size (Å)	$dT/dz(K/\text{Å})$	$\kappa(WK^{-1}m^{-1})$
500	116	-0.2483	29.2090	111	-0.2321	31.2477
600	119	-0.3230	26.8058	113	-0.3569	24.2597
800	120	-0.5120	22.3884	115	-0.5851	19.5913
1000	123	-0.9607	15.3179	118	-0.6806	21.6216

Table 6. The grain size, temperature gradient dT/dz , and thermal conductivity κ , at different temperatures for (200) and (220) oriented grains in the system with supercell 15.3601 X 15.3601 X 550.

(200) oriented grains				(220) oriented grains		
Temperature (K)	Grain size (Å)	$dT/dz(K/\text{Å})$	$\kappa(WK^{-1}m^{-1})$	Grain size (Å)	$dT/dz(K/\text{Å})$	$\kappa(WK^{-1}m^{-1})$
500	250	-0.1633	43.0820	234	-0.1655	42.5093
600	257	-0.2346	35.8067	238	-0.2229	37.6861
800	258	-0.3908	28.4109	242	-0.3533	31.4265
1000	259	-0.7429	18.9584	243	-0.4781	29.4586

Table 7. The grain size, temperature gradient dT/dz , and thermal conductivity κ , at different temperatures for (200) and (220) oriented grains in the system with supercell 11.52 X 11.52 X 570.

Temperature (K)	(200) oriented grains			(220) oriented grains		
	Grain size (Å)	$dT/dz(K/\text{Å})$	$\kappa(WK^{-1}m^{-1})$	Grain size (Å)	$dT/dz(K/\text{Å})$	$\kappa(WK^{-1}m^{-1})$
500	257	-0.1934	51.1874	260	-0.2119	46.7184
600	262	-0.2815	42.4583	262	-0.2902	41.1854
800	266	-0.5080	30.2294	269	-0.4761	32.2548
1000	270	-0.8954	22.0628	272	-0.6774	26.5194

Table 8. The grain size, temperature gradient dT/dz , and thermal conductivity κ , at different temperatures for (200) and (220) oriented grains in the system with supercell 11.52 X 11.52 X 680.

Temperature (K)	(200) oriented grains			(220) oriented grains		
	Grain size (Å)	$dT/dz(K/\text{Å})$	$\kappa(WK^{-1}m^{-1})$	Grain size (Å)	$dT/dz(K/\text{Å})$	$\kappa(WK^{-1}m^{-1})$
500	317	-0.2915	54.5233	317	-0.2440	65.5233
600	319	-0.3946	47.6362	318	-0.3269	57.5014
800	320	-0.7134	33.1348	321	-0.5212	45.3538
1000	322	-1.3540	22.0947	334	-0.6933	43.1505

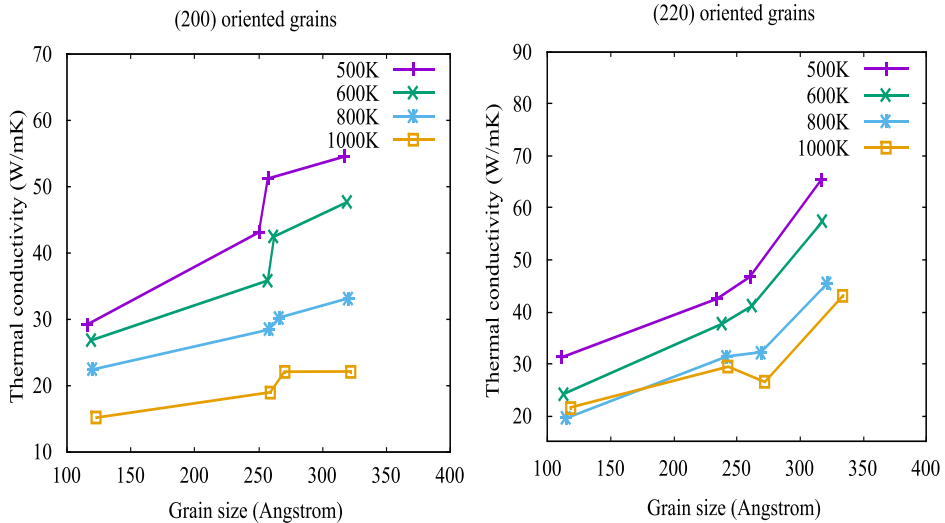


Figure 4. Grain size dependence of the grain thermal conductivity for (200) and (220) oriented grains

In the (200) crystallographic oriented region, the grain sizes considered are 111, 234, 260 and 317 Å at 500K, and the corresponding grain thermal conductivity is 31.2477, 42.5093, 46.7184 and 65.5233 W/mK. At 600K, we obtained 24.2597, 37.6861, 41.1854 and 57.5014 W/mK as the grain thermal conductivity for grain

sizes 113, 238, 262 and 318 Å. Around 800K, we calculated 19.5913, 31.4265, 32.2548 and 45.3538 W/mK for grain sizes 115, 242, 269 and 321 Å. Finally, at 1000K, we calculated 21.6216, 29.4586, 26.5194 and 43.1505 W/mK for grain sizes 118, 243, 272 and 334 Å. From the aforementioned, it is clear that, as the grain size is increased, the

grain thermal conductivity increased substantially for all grain crystallographic orientation types and temperatures as displayed in Figure 4. The reason for these is that the phonons or lattice waves are scattered near the grain interface. The extent of increase in thermal conductivity is more significant around grain size 317 Å at 500K for both (200) and (220) crystallographic oriented grains, as shown by the purple curve in Figure 4.

It is important to state that results for thermal conductivity obtained from

this study are comparably smaller than the bulk thermal conductivity for silicon at 500, 600, 800 and 1000K reported by Howell [30] using the same Stillinger-Weber potential. This trend is expected since the bulk thermal conductivity is generally higher than the corresponding grain thermal conductivity [31]. This is because the mean free path of phonons is normally larger than 1×10^4 Å, which implies that the simulated smaller grain size suppresses the thermal conductivity [30, 31].

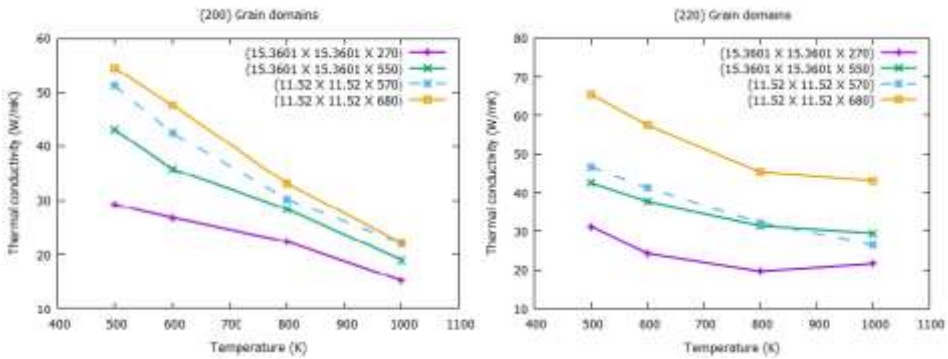


Figure 5. Temperature dependence of the grain thermal conductivity for (200) and (220) oriented grains

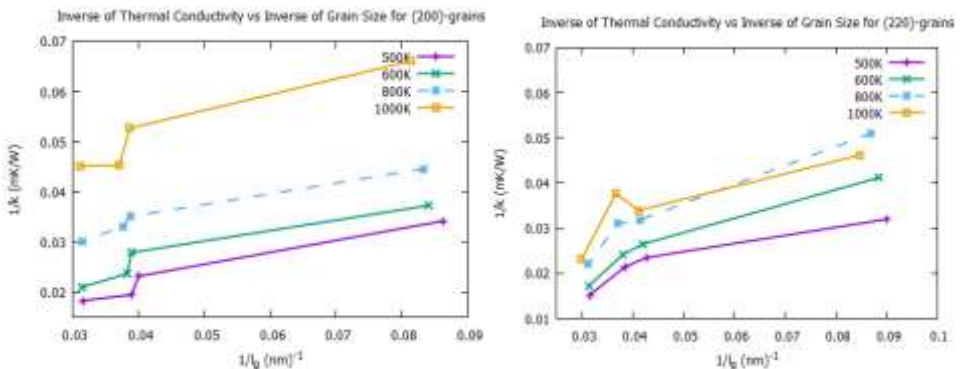


Figure 6. Inverse of thermal conductivity versus inverse of grain size for both (200) and (220) oriented grains.

From Tables 5 – 8, it is also clear that the grain thermal conductivity decreased substantially when the temperature is increased as displayed

in Figure 5. These results indicate that simulation size and temperature have great influence on thermal conductivity of materials, which

signifies a positive beneficial effect of grain size and temperature, especially in the micro and nanoelectronic device industries. It is important to note that this behavior has been observed by other researchers using different techniques [32, 33]. Furthermore, Figure 6 displays a plot of the inverse of thermal conductivity against the inverse of grain size. In RNEMD simulations phonons are scattered in the hot and cold regions. Usually, this leads to a lower mean free path, and lower thermal conductivity. It is customary to perform simulations for cells of different sizes to overcome this problem, as has been done by other researchers [34, 35]. Calculating thermal conductivity (κ) for different grain sizes and plotting the inverse of κ against the inverse of l_g , it is also possible to extrapolate $l_g = 0$ to determine the thermal conductivity of a simulation of infinite grain size which is comparable to infinite system data [30, 36]. This accounts for the fictitious phonon-boundary scattering introduced by the heat transfer dynamics.

Conclusion

References

1. Quantumwise Document, www.quantumwise.com.
2. Goddard W. (Ed.), Brenner, D. (Ed.), Lyslevski, S. (Ed.) and Lafrate, G. (Ed.), (2012). *Handbook of NanoScience, Engineering, and Technology*, Third Edition, Boca Raton: CRC Press.
3. Gu, J., Yang, X., Lv, Z., Li, N., Liang, C. Zhang, Q. (2016). Functionalized graphite nanoplatelets/epoxy resin nanocomposites with high thermal conductivity, *International Journal of Heat and Mass Transfer* 92, 15-22.
4. Simon, R.P. and Alan, J.H.M. (2005). *Introduction to Thermal Transport*, Elsevier Materials Today, 18 – 20.
5. International Technology Roadmap for Semiconductors: ITRS Reports, <http://www.itrs.net/reports.html>.
6. Ferain, I., Colinge, C.A. and Colinge, J. (2011). Multigate transistors as the future of classical metal-oxide-semiconductor field-effect

- transistors, *Nature*, 479, 310 – 316.
7. Schelling, P.K., Shib, L. and Goodson, K.E. (2005). Managing heat for electronics, *Mater. Today*8 (6), 30-35.
 8. Pop, E., Sinha, S. and Goodson, K. E. (2006). Heat Generation and Transport in Nanometer-Scale Transistors, *Proceedings of the IEEE*, 94 (8), 1587-1601.
 9. Haensch, W., Nowak, E.J., Dennard, R.H., Solomon, P.M., Bryant, A., Dokumaci, O.H., Kumar, A., Wang, X., Johnson, J.B. and Fischetti, M.V. (2006). Silicon CMOS devices beyond scaling, *IBM Journal of Research and Development*, 50, 339-361.
 10. Arden L.M., and Li S. (2014). Emerging challenges and materials for thermal management of electronics, *Elsevier: Materials Today*17 (4), 163 – 174.
 11. Datacom Equipment Power Trends and Cooling Applications, 2nd ed., ASHRAE, Atlanta, GA, 2012.
 12. na.industrial.panasonic.com/PGS. The Advance Thermal Management Solution for Today's Designs.
 13. Tang, B., Hu, G., Gao, H. and Hai, L. (2015). Application of graphene as filler to improve thermal transport property of epoxy resin for thermal interface materials, *International Journal of Heat and Mass Transfer*,85, 420–429.
 14. Siemens, M.E., Li, Q., Yang, R., Nelson, K.A., Anderson, E.H., Murnane, M.M. and Kapteyn, H.C. (2010). Quasi-ballistic thermal transport from nanoscale interfaces observed using ultrafast coherent soft x-ray beams, *Nature Mater.* 9, 26–30.
 15. Müller-Plathe, F. (1997). A simple nonequilibrium molecular dynamics method for calculating the thermal conductivity *J. Chem. Phys.* 106 (14), 6082-6085.
 16. Carlos, N. and Avalos, J.B. (2003). Non-equilibrium exchange algorithm for molecular dynamics simulation of heat flow in multicomponent systems, *Mol. Phys.* 101 (14), 2303 – 2307.
 17. Schelling, P.K. (2004). Kapitza conductance and phonon scattering at grain boundaries by simulation, *Journal of Applied Physics*,95, 6082 – 6091.
 18. Stackhouse, S. and Stixrude L. (2010). Theoretical Methods for Calculating the Lattice Thermal Conductivity of Minerals, *Reviews of Mineralogy and Geochemistry*, 71, 253-269.
 19. Atomistix ToolKit 2017.1, Quantumwise A/S, www.quantumwise.com.
 20. Griebel, M., Knapek, S. and Zumbusch, G. (2007). *Numerical Simulation in Molecular Dynamics*, Springer.
 21. Griebel, M. and Hamaekers, J., (2004). *Computer Methods in Applied Mechanics and Engineering*, 193, 1773-1788.
 22. Stillinger, F.H. and Weber, T.A. (1985). Computer Simulation of local order in condensed phases of silicon, *Phys. Rev. B*, 31, 5262 – 5271.

23. Zhu, C., Byrd, R.H., Lu, P., and Nocedal, J. (1997). Algorithm 778: L-BFGS-B: Fortran subroutines for large-scale bound-constrained optimization, *ACM Transactions on Mathematical Software* 23 (4), 550 – 560.
24. Martyna, G.J., Tobias, D.J. and Klein, M.L. (1994). Constant pressure molecular dynamics algorithms, *J. Chem. Phys.*, 101 (5):4177–4189.
25. Martyna, G. J., Klein, M. L. and Tuckerman, M. (1992). Nosé–hoover chains: The canonical ensemble via continuous dynamics. *J. Chem. Phys.*, 97 (4), 2635–2643.
26. Kapitza, P.L. (1941). Heat Transfer and Superfluidity of Helium II, *Phys. Rev.* 60, 354.
27. Robert J.S., Leonid, V.Z. and Norris, P.M. (2007). Effects of temperature and disorder on thermal boundary conductance at solid-solid interfaces: Nonequilibrium molecular dynamics simulations, *International Journal of Heat and Mass Transfer*, 50, 3977–3989.
28. Song, G. and Min, C. (2013). Temperature dependence of thermal resistance at a solid/liquid interface, *International Journal at the Interface between Chemistry and Physics*, 111, 903-908.
29. Nika, D.L., Askerov, A.S. and Balandin, A.A. (2012). Anomalous Size Dependence of the Thermal Conductivity of Graphene Ribbons, *Nano Letters* 12 (6), 3238–3244.
30. Howell P.C. (2012). Comparison of molecular dynamics methods and interatomic potentials for calculating the thermal conductivity of silicon, *J Chem Phys.* 137 (22), 224111.
31. Akbar, B., Sang-Pil, K., Rodney, S.R., and Vivek, B.S. (2011). Thermal transport across Twin Grain Boundaries in Polycrystalline Graphene from Nonequilibrium Molecular Dynamics Simulations, *Nano Lett.*, 11, 3917–3921.
32. Sebastian G.V. and Gang C. (2000). Molecular-dynamics simulation of thermal conductivity of silicon crystals, *Phys. Rev. B* 61, 2651.
33. Mark S.H. and Steven G.L. (1986). Electron correlation in semiconductors and insulators: Band gaps and quasiparticle energies, *Phys. Rev. B* 34, 5390.
34. Stackhouse, S., Stixrude L. and Karki B.B. (2010), Thermal Conductivity of Periclase (MgO) from first principle, *Phys. Rev. Lett.* 104, 208501.
35. Patrick K.S, Simon R.P, and Pawel K. (2002). Comparison of atomic-level simulation methods for computing thermal conductivity, *Phys. Rev. B* 65, 144306.
36. Sellan, D.P., Landry, E.S., Turney, J. E., McGaughey, A.J.H. and Amon, C.H. (2010). Size effects in molecular dynamics thermal conductivity predictions, *Phys. Rev. B* 81, 214305